Evidence of Topological Nodal-Line Fermions in ZrSiSe and ZrSiTe

Jin Hu, Zhijie Tang, Jinyu Liu, Xue Liu, Yanglin Zhu, David Graf, Kevin Myhro, Son Tran, Chun Ning Lau, Jiang Wei, and Zhiqiang Mao

Phys. Rev. Lett. **117**, 016602 — Published 30 June 2016

DOI: 10.1103/PhysRevLett.117.016602

Evidence of topological nodal-line fermions in ZrSiSe and ZrSiTe

Jin Hu[1†], Zhijie Tang[1†], Jinyu Liu[1], Xue Liu[1], Yanglin Zhu[1], David Graf[2], Kevin Myhro[3], Son Tran[3], Chun Ning Lau[3], Jiang Wei[1] and Zhiqiang Mao[1*]

[1]Department of Physics and Engineering Physics, Tulane University, New Orleans, LA 70118, USA

[2]National High Magnetic Field Lab, Tallahassee, FL 32310, USA

[3]Department of Physics, University of California, Riverside, CA 92521, USA

Abstract

Dirac nodal-line semimetal, which represents a new quantum state of topological materials, has been experimentally realized only in a few systems, including $PbTaSe_2$, $PtSn_4$ and ZrSiS. In this letter, we report evidence of nodal-line fermions in ZrSiSe and ZrSiTe probed in de Haas–van Alphen quantum oscillations. Although ZrSiSe and ZrSiTe share similar layered structure with ZrSiS, our studies show the Fermi surface (FS) enclosing Dirac nodal-line is of 2D character in ZrSiTe, in contrast with 3D-like FS in ZrSiSe and ZrSiS. Another important property revealed in our experiment is that the nodal-line fermion density in this family of material (~ 10^{20} cm^{-3}) is much higher than the Dirac fermion density of other topological materials with discrete nodes. In addition, we have demonstrated ZrSiSe and ZrSiTe single crystals can be thinned down to 2D atomic thin layers through microexfoliation, which offers the first platform to explore exotic properties of topological nodal-line fermions in low dimensions.

[†]J.H. and Z.T. equally contributed to this work.

[*]zmao@tulane.edu

The recently discovered three-dimensional (3D) topological semimetals, including Dirac, Weyl and topological nodal-line semimetals, have attracted intensive attentions due to their exotic properties such as high charge carrier mobility [1-2], large magnetoresistance [1], and potential topological superconductivity [3]. In 3D Dirac semimetals such as Na_3Bi [4-5] and Cd_3As_2 [6-10], four-fold degenerate linear band crossings at Dirac nodes occur at discrete momentum points. With lifted spin degeneracy by either broken time reversal or spatial inversion symmetry, each Dirac cone splits into a pair of Weyl cones with opposite chirality [4, 6, 11-12]. The Weyl state due to broken inversion symmetry was first demonstrated in transition metal monopnictides [13-18] and signatures of time reversal symmetry breaking Weyl state was recently found in $YbMnBi_2$ [19]. For topological nodal-line semimetals, Dirac band crossings take place along a one-dimensional line/loop, contrasted with discrete Dirac points in Dirac or Weyl semimetals. The experimentally established examples include $PbTaSe_2$ [20], $PtSn_4$ [21] and ZrSiS [22-23].

Among the reported nodal-line semimetals, ZrSiS was found to have distinct properties. First, in addition to the nodal-line Dirac crossings, it also harbors a new type of Dirac state protected by the non-symmorphic symmetry [22, 24]. Second, its Dirac bands are linearly dispersed in a wide energy range up to 2eV, much larger than that of other known Dirac materials [22]. Third, unusual surface states hybridized with bulk bands have also been observed [22]. Moreover, surprisingly strong Zeeman splitting has been observed in the de Haas–van Alphen (dHvA) effect [25]. These fascinating properties motivated us to investigate isostructural compounds ZrSiSe and ZrSiTe. These compounds belong to a large family of materials WHM with the PbFCl-type structure (W=Zr/Hf/La, H=Si/Ge/Sn/Sb, M=O/S/Se/Te). The first-principle calculations [26] have shown that these isostructural compounds have similar electronic

structures. The two-dimensional (2D) topological insulator (TI), which was proved only in a few artificial systems such as HgTe/CdTe [27-28] and InAs/GaSb [29] quantum wells, can possibly be realized in monolayer WHM [26]. Recent ARPES studies on ZrSnTe has provided evidence for the TI band structure on the top layer [30]. Since ZrSiM possesses layered structure and the interlayer bonding energy decreases by two orders of magnitude as M varies from O to Te [26], monolayer thin films may be accessible through microexfoliation for ZrSiSe and ZrSiTe. If this proves to be true, these materials would provide a rare opportunity to investigate 2D TIs [26].

In this letter, we report evidence of nodal-line fermions in ZrSiSe and ZrSiTe probed in quantum oscillations and demonstrate the accessibility of atomically thin layers of these materials. We will also show that ZrSiSe shares a similar 3D-like Fermi surface (FS) with ZrSiS, whereas the FS of ZrSiTe displays a more remarkable 2D-like signature though a 3D-like component also exists. Our findings not only pave a way to further understand novel exotic properties of the nodal-line semimetals, but also highlight a new possible route to realize 2D TIs.

The plate-like ZrSiSe and ZrSiTe single crystals (insets of Figs. 1b and 1d) were synthesized using a chemical vapor transport method as stated in the Supplementary Material [31]. The excellent crystallinity is demonstrated by the sharp (00L) X-ray diffraction peaks (Fig. 1 in the Supplementary Material [31]). As shown in Fig. 1a, all ZrSiM (M=S/Se/Te) compounds share a similar tetragonal structure formed from the stacking of M-Zr-Si-Zr-M slabs [35]; the slab thickness along the *c*-axis is increased by 4% and 18% for ZrSiSe and ZrSiTe respectively, as compared to ZrSiS (Fig. 1 in the Supplementary Material [31]). This is caused by the increased ionic radius from S to Te ions, which also results in the structural dimensionality evolution from 3D to 2D [26, 35].

In spite of reduced dimensionality, ZrSiSe and ZrSiTe also host nodal-line fermions, which has been evidenced by our quantum oscillation experiments. In Figs. 1b-d, we present the isothermal magnetization measured up to 7T for ZrSiSe (Figs. 1c-1d) and ZrSiTe (Fig. 1b). In ZrSiSe, both the out-of-plane ($B//c$, Fig. 1c) and in-plane ($B//ab$, Fig. 1d) magnetizations exhibit strong dHvA oscillations at low temperatures. Similar features were also observed in nodal-line semimetal ZrSiS whose FS enclosing the nodal-line has been shown to be of 3D character [25]. Such a similarity implies that the FS of ZrSiSe is also of a 3D character. In ZrSiTe, however, strong quantum oscillations are present for $B//c$ (Fig. 1b), but hardly seen for $B//ab$, suggesting that ZrSiTe may have a 2D-like FS. More detailed discussions on the evolution of FS from ZrSiS to ZrSiTe will be given below.

From the analyses of dHvA oscillations, we have seen typical signatures of Dirac fermions in both ZrSiSe and ZrSiTe. We first focus on ZrSiSe whose lattice structure only slightly differs from that of ZrSiS. In Figs. 2a and 2d, we present the oscillatory components of magnetization for ZrSiSe, obtained after subtracting the background. Strong oscillations with the amplitudes of 1~2 emu/mol at T=1.8K are clearly seen for both $B//c$ (Fig. 2a) and $B//ab$ (Fig. 2d). From the Fast Fourier transformation (FFT) analyses, we have derived a single frequency of 210T for the out-of-plane oscillations (Fig. 2b, inset), which is comparable with the dHvA frequency F_β (=240T) probed in ZrSiS for the same field orientation [25]. Nevertheless, another very small dHvA frequency (F_α=8.4T) for $B//c$ in ZrSiS was not observed in ZrSiSe. This implies that the FSs of ZrSiS and ZrSiSe have somewhat different morphologies though both share a common 3D-like character. In contrast with the single-frequency oscillations for $B//c$, the in-plane dHvA oscillation pattern (Fig. 2d) exhibits a superposition of low- and high-frequency oscillations. In Fig. 2f we have separated the low (upper panel) and high (lower panel) frequency

components. Both components display beat patterns, indicating multiple frequencies for each. Indeed, FFT analyses (Fig. 2e, inset) have revealed three major low frequencies (19.2T, 22.8T, and 24T) and three major high frequencies (126.9T, 132.7T, and 142T). Multiple frequencies under in-plane field have also been observed in ZrSiS [25], which is suggestive of 3D-like electronic structure.

In general, the oscillatory magnetization of a Dirac system can be described by the Lifshitz-Kosevich (LK) formula [36-37] with Berry phase being taken into account [38]:

$$\Delta M \propto -B^{\lambda} R_T R_D R_S \sin[2\pi(\frac{F}{B} + \gamma - \delta)] \qquad (1)$$

where $R_T = \alpha T\mu/B\sinh(\alpha T\mu/B)$, $R_D = \exp(-\alpha T_D\mu/B)$, and $R_S = \cos(\pi g\mu/2)$. μ is the ratio of effective cyclotron mass m^* to free electron mass m_0. T_D is Dingle temperature, and $\alpha = (2\pi^2 k_B m_0)/(\hbar e)$. The oscillation of ΔM is described by the sine term with a phase factor $\gamma - \delta$, in which $\gamma = \frac{1}{2} - \frac{\phi_B}{2\pi}$ and ϕ_B is Berry phase. The phase shift δ is determined by the dimensionality of FS; δ=0 and ±1/8, respectively, for 2D and 3D cases. In addition, the exponent λ is also determined by the dimensionality; λ=1/2 and 0 for 3D and 2D cases, respectively. From the LK formula, the effective mass m^* can be obtained through the fit of the temperature dependence of the oscillation amplitude to the thermal damping factor R_T, as shown in Figs. 2b and 2e. For all probed oscillation frequencies, the obtained effective masses are in the range of 0.04-0.08m_0 (see Table 1), which are comparable to that of ZrSiS [25] and Cd_3As_2 [2, 39-40]. Using the fitted effective mass as a known parameter, we can further fit the oscillation patterns at a given temperature (*e.g.* T=1.8K) to the LK formula (Eq. 1), from which quantum mobility and Berry phase can be extracted. Given that the FS of ZrSiSe is of a strong 3D character as discussed

below, we have adopted the 3D LK formula, which describes the out-of-plane dHvA oscillations very well (Fig. 2c). The fitted Dingle temperature T_D is 5.6 K, which corresponds to the quantum relaxation time $\tau_q = \hbar/(2\pi k_B T_D) = 2.2\times10^{-13}$ s and quantum mobility $\mu_q = e\tau/m^* = 4605$ cm^2/(Vs). The LK fit also yields a phase factor $\gamma - \delta$ of 0.47, from which the Berry phase ϕ_B is determined to be 0.31π for $\delta = -1/8$ and -0.19π for $\delta = 1/8$. Similar Berry phase can also be obtained from the commonly used Landau level fan diagram (Fig. 2 in the Supplementary Material [31]). Although this Berry phase is deviated from the expected value of π, we have probed Berry phases very close to π in the dHvA oscillations under $B//ab$, as shown below. Such a variation may be associated with the FS anisotropy.

For the in-plane, multi-frequency oscillations, the fits have to be done using the multiband LK formula [25, 41]. In order to achieve more accurate fits, we have separated the low- and high- frequency components and fit them individually, as shown in Fig. 2f. These fits yield the Dingle temperatures of 5-15K, as shown in Table 1. Combined with the effective masses obtained in Fig. 2e, we have derived quantum mobility ranging from 2500 to 9500 cm^2/Vs for various frequencies (Table 1). Additionally, from these fits, we also obtained non-trivial Berry phase for each band for $\delta = \pm 1/8$, with several of them being close to π (see Table 1). These results indicate that electrons involved in the in-plane quantum oscillations are also Dirac electrons, similar to the observations in ZrSiS [25].

To make a more comprehensive comparison between ZrSiS and ZrSiSe, we have systematically investigated the variation of the oscillation frequencies of ZrSiSe with the magnetic field orientation (see the inset of Fig. 4b for the experiment setup). As presented in Fig. 4a, after the background subtraction, the oscillation patterns display a clear evolution with the rotation of magnetic field. In Fig. 4c we present the oscillation frequencies extracted from the

FFT analyses (Fig. 3a in the Supplementary Material [31]). Overall, we have observed three major frequency branches. With increasing the angle θ, the highest frequency branch (F_β) continues to increase until it disappears above 65°. This trend can be described by $F_{2D}/\cos\theta + F_{3D}$ which includes both 2D and isotropic 3D FS components, with the relative weight $F_{2D}/F_{3D} \approx 0.8$. This indicates that the dimensionality of the FS associated with F_β is between 2D and 3D. In addition to F_β, another two low frequency branches with weak angular dependences (F_η and F_α) are also present for $45° < \theta < 90°$, indicating a 3D component of the FS. Such angular dependences of F_β, F_η and F_α in ZrSiSe have also been verified by the Shubnikov-de Haas (SdH) effects. The SdH oscillations, though much weaker than the dHvA oscillations, can be observed in high field magnetotransport measurements (Fig. 5 in the Supplementary Material [31]). The oscillation frequencies extracted from FFT spectra (Fig. 6 in the Supplementary Material [31]) are in good agreement with the results probed in the dHvA oscillations, as shown in Fig.4c.

In our previous dHvA studies on ZrSiS [25], we observed angular dependences of frequencies similar to F_β and F_η seen in ZrSiSe. However, the lowest frequency branch $F_\alpha(\theta)$ is distinct between ZrSiS and ZrSiSe. F_α of ZrSiS shows a continuous evolution from $\theta = 0°$ to 90° and can be fitted to $F_\alpha(\theta=0)/\cos\theta$ in low angle region ($0° < \theta < 62°$), but becomes weakly angle dependent for $62° < \theta < 90°$. This suggests that the FS associated with F_α in ZrSiS is of a striking 2D character though a 3D component also exists [25]. In contrast, $F_\alpha(\theta)$ of ZrSiSe is present only in the $45° < \theta < 90°$ range and remains nearly constant (Fig. 4c), indicating the F_α FS of ZrSiSe has distinct morphology from that of ZrSiS. APRES studies have shown that the FS of ZrSiS consists of four lens-shaped Fermi pockets surrounding the Γ point and small electron pockets at X [22-23]. The Dirac nodal-lines are enclosed by the lens-shaped pockets, while the electron pocket at X involves hybridization of surface states and bulk bands [22]. The high oscillation frequency F_β

in ZrSiS is found to arise from the lens-shaped pockets, while the low frequency F_α corresponds to the small electron pocket at X [25]. Given similar electronic structures between ZrSiS and ZrSiSe [26], we can reasonably expect existence of similar lens-shaped Fermi pocket enclosing Dirac nodal-line in ZrSiSe. The F_β and F_η branches of ZrSiSe (Fig. 4c) most likely correspond to the expected nodal-line FS, similar to the scenario in ZrSiS [25]. On the other hand, although the major features of band structures are similar between ZrSiS and ZrSiSe, replacing S with Se should more or less modify the FS. This may explain distinct characteristics of F_α between these two compounds.

Next we discuss our results obtained on ZrSiTe. Although ZrSiSe preserves major quantum oscillation properties of ZrSiS as discussed above, we expect more significant electronic structure modifications in ZrSiTe due to the greatly reduced interlayer coupling [26]. This is indeed manifested in our experiments. In ZrSiTe, we observed striking dHvA oscillations for *B//c*, but not for *B//ab*, suggesting quasi-2D electronic structure. Following the approach used for analyzing dHvA effect in ZrSiSe, we have extracted the oscillatory component of the out-of-plane magnetization for ZrSiTe (Fig. 3a), and determined the oscillation frequencies to be 102T and 154T from its FFT spectrum (Fig. 3b, inset). The effective masses corresponding to these two frequencies are found to be $0.093m_0$ and $0.091m_0$, respectively (Fig. 3b). From ZrSiS to ZrSiSe and to ZrSiTe, Dirac fermions becomes more massive (Table 1), which can probably be associated with the enhanced particle-hole asymmetry [26] and larger spin-orbit coupling-induced gap at the nodal-line. The fit of the oscillation pattern to the 3D LK formula (Fig. 3c) yields quantum mobility of 1625 cm^2/Vs (940 cm^2/Vs) for the 102T (154T) component as well as non-trivial Berry phases as listed in Table 1. Since the FS of ZrSiTe is of 2D character as we show below, we also fitted the oscillation pattern to the 2D LK formula, which yields slightly

larger Dingle temperature but similar phase factor (Fig. 4 in the Supplementary Material [31]). These results indicate that electrons participating in quantum oscillations in ZrSiTe are also Dirac fermions.

Given that similar band structures have been predicted for all ZrSiM compounds [26] and the dHvA frequency of 154T probed in ZrSiTe is not far from F_β probed in ZrSiS (240T) and ZrSiSe (210T) for $B//c$, the FS associated with F_β, which encloses nodal-lines, is most likely preserved in ZrSiTe. To examine the FS morphology of ZrSiTe, we have also investigated the evolution of dHvA oscillations with the field orientation and found that the oscillatory component of magnetization is gradually suppressed with increasing θ and becomes non-observable for θ>45˚ (Fig. 4b). Fig. 4d shows the evolution of oscillation frequencies extracted from the FFT analyses (Fig. 3b in the Supplementary Material [31]). The higher frequency component exhibits a weak angular-dependence, while the lower one shows a clear variation with θ and can be fitted to $F_{2D}/\cos\theta + F_{3D}$ as illustrated by the red curve. The relative weight between 2D and 3D components derived from the fit, F_{2D}/F_{3D} is ≈1.7, about twice as large as that of ZrSiSe (F_{2D}/F_{3D} ≈0.8), implying that the FS of ZrSiTe is of a 2D character though a 3D component also exists. The 2D-like FS of ZrSiTe is in line with its reduced interlayer binding energy as indicated above [26, 35] and is further supported by our measurements of angular-resolved magnetoresistance (AMR). As seen in Fig. 4e, the AMR data of ZrSiTe, measured with the current being applied within the plane and the field being rotated in a manner shown in the inset of Fig. 4b ($B//I$ for θ=90°), exhibits a typical two-fold anisotropy expected for a material with 2D/quasi-2D electronic structure and classical Lorentz-type magnetoresistance where AMR$\propto(B\cos\theta)^2$. In contrast, ZrSiSe with a 3D-like FS exhibits "butterfly-shaped" AMR (Fig. 4e), similar to that seen in ZrSiS [42-43].

In general, nodal-line semimetals are expected to have high Dirac fermion density due to Dirac band crossings along a line/loop. Indeed, this has been observed in our transport measurements. From the simultaneously fitting for magnetoresistivity and Hall resistivity using a two-band model [44], both electron (n_e) and hole (n_h) densities are estimated to be ~10^{20} cm^{-3} for both ZrSiSe and ZrSiTe (Figs. 7 and 8 in the Supplementary Material [31]), significantly higher than those of other Dirac systems such as Cd_3As_2 (~10^{18} cm^{-3} [1-2, 39]) and Na_3Bi (~10^{17} cm^{-3} [45]), topological insulators (~$10^{10\text{-}12}$ cm^{-3} [46]), and graphene ($10^{10\text{-}12}$ cm^{-3} [47-48]), but comparable to that of nodal-line semimetal ZrSiS (n_e, n_h ~10^{20} cm^{-3}) [25] for which only the Dirac bands cross the Fermi level [22]. Given that ZrSiM (M=S/Se/Te) compounds share similar bulk electronic structures [26], we can reasonably expect that the high carrier density in ZrSiSe and ZrSiTe also reflects the nature of Dirac band crossings along a nodal-line. Therefore, the high Dirac fermion density not only provides additional support for the nodal-line state in ZrSiSe and ZrSiTe, but also explains the observation of significant dHvA oscillations in these materials.

As indicated above, the weak interlayer bonding of ZrSiSe and ZrSiTe implies the possibility that their atomically thin layers can be obtained through mechanical exfoliation. We have demonstrated their 2D atomic crystals are indeed accessible through microexfoliation. As shown in Supplementary Material (Fig. 9 in the Supplementary Material) [31], in our initial trials, we have already obtained ZrSiSe and ZrSiTe nano-flakes with their thickness less than 10 nm. Therefore, these compounds hold great potential to realize the theoretically predicted 2D TIs in monolayer WHM [26]. Furthermore, considering the exceptionally high Dirac fermion density, these compounds also has a potential to fill the gap between the important fundamental physics of topological materials and their practical quantum device applications.

Acknowledgement

This work was supported by the US Department of Energy under grant DE-SC0014208 (support for personnel, material synthesis and magnetization measurements). The work at the NHMFL is supported by the NSF Cooperative Agreement No. DMR-1157490 and the State of Florida (transport measurements under high magnetic fields). The wok at University of California-Riverside is supported by DOE BES Division under grant no. ER 46940-DE-SC0010597 (high field magnetoresistance measurements).

References

[1] T. Liang, Q. Gibson, M. N. Ali, et al., *Nature Mater.* **14**, 280-284 (2015)

[2] Y. Zhao, H. Liu, C. Zhang, et al., *Phys. Rev. X* **5**, 031037 (2015)

[3] H. Wang, H. Wang, H. Liu, et al., *Nature Mater.* **15**, 38-42 (2016)

[4] Z. Wang, Y. Sun, X.-Q. Chen, et al., *Phys. Rev. B* **85**, 195320 (2012)

[5] Z. K. Liu, B. Zhou, Y. Zhang, et al., *Science* **343**, 864-867 (2014)

[6] Z. Wang, H. Weng, Q. Wu, et al., *Phys. Rev. B* **88**, 125427 (2013)

[7] Z. K. Liu, J. Jiang, B. Zhou, et al., *Nature Mater.* **13**, 677-681 (2014)

[8] M. Neupane, S.-Y. Xu, R. Sankar, et al., *Nature Commun.* **5**, 3786 (2014)

[9] H. Yi, Z. Wang, C. Chen, et al., *Sci. Rep.* **4**, 6106 (2014)

[10] S. Borisenko, Q. Gibson, D. Evtushinsky, et al., *Phys. Rev. Lett.* **113**, 027603 (2014)

[11] H. Weng, C. Fang, Z. Fang, et al., *Phys. Rev. X* **5**, 011029 (2015)

[12] S.-M. Huang, S.-Y. Xu, I. Belopolski, et al., *Nature Commun.* **6**, 7373 (2015)

[13] S.-Y. Xu, I. Belopolski, N. Alidoust, et al., *Science* **349**, 613-617 (2015)

[14] L. X. Yang, Z. K. Liu, Y. Sun, et al., *Nature Phys.* **11**, 728-732 (2015)

[15] B. Q. Lv, N. Xu, H. M. Weng, et al., *Nature Physics* **11**, 724–727 (2015)

[16] B. Q. Lv, H. M. Weng, B. B. Fu, et al., *Phys. Rev. X* **5**, 031013 (2015)

[17] S.-Y. Xu, N. Alidoust, I. Belopolski, et al., *Nature Phys.* **11**, 748-754 (2015)

[18] N. Xu, H. M. Weng, B. Q. Lv, et al., *Nature Commun.* **7**, 11006 (2015)

[19] S. Borisenko, D. Evtushinsky, Q. Gibson, et al., *arXiv:1507.04847* (2015)

[20] G. Bian, T.-R. Chang, R. Sankar, et al., *Nature Commun.* **7**, 10556 (2016)

[21] Y. Wu, L.-L. Wang, E. Mun, et al., *Nature Phys.* advance online publication, Doi:10.1038/nphys3712

[22] L. M. Schoop, M. N. Ali, C. Straszer, et al., *Nature Commun.* **7**, 11696 (2016)

[23] M. Neupane, I. Belopolski, M. M. Hosen, et al., *Phys. Rev. B* **93**, 201104 (2016)

[24] S. M. Young and C. L. Kane, *Phys. Rev. Lett.* **115**, 126803 (2015)

[25] J. Hu, Z. Tang, J. Liu, et al., *arXiv:1604.01567* (2016)

[26] Q. Xu, Z. Song, S. Nie, et al., *Phys. Rev. B* **92**, 205310 (2015)

[27] B. A. Bernevig, T. L. Hughes and S.-C. Zhang, *Science* **314**, 1757-1761 (2006)

[28] M. König, S. Wiedmann, C. Brüne, et al., *Science* **318**, 766-770 (2007)

[29] I. Knez, R.-R. Du and G. Sullivan, *Phys. Rev. Lett.* **107**, 136603 (2011)

[30] R. Lou, J.-Z. Ma, Q.-N. Xu, et al., *arXiv:1601.07294* (2016)

[31] See Supplemental Material at [url], which includes Ref. [32-34].

[32] J. Xiong, Y. Luo, Y. Khoo, et al., *Phys. Rev. B* **86**, 045314 (2012)

[33] A. A. Abrikosov, *Phys. Rev. B* **58**, 2788-2794 (1998)

[34] A. A. Abrikosov, *Fundamentals of the Theory of Metals*. (North-Holland, Amsterdam, 1988)

[35] C. Wang and T. Hughbanks, *Inorg. Chem.* **34**, 5524-5529 (1995)

[36] I. M. Lifshitz and A. M. Kosevich, *Sov. Phys. JETP* **2**, 636-645 (1956)

[37] D. Shoenberg, *Magnetic Oscillations in Metals*. (Cambridge Univ. Press, Cambridge, 1984)

[38] G. P. Mikitik and Y. V. Sharlai, *Phys. Rev. Lett.* **82**, 2147-2150 (1999)

[39] L. P. He, X. C. Hong, J. K. Dong, et al., *Phys. Rev. Lett.* **113**, 246402 (2014)

[40] A. Narayanan, M. D. Watson, S. F. Blake, et al., *Phys. Rev. Lett.* **114**, 117201 (2015)

[41] J. Hu, J. Y. Liu, D. Graf, et al., *Sci. Rep.* **6**, 18674 (2016)

[42] M. N. Ali, L. M. Schoop, C. Garg, et al., *arXiv:1603.09318* (2016)

[43] X. Wang, X. Pan, M. Gao, et al., *arXiv:1604.00108* (2016)

[44] C. M. Hurd, *The Hall Effect in Metals and Alloys*. (Cambridge University Press, Cambridge, 1972)

[45] J. Xiong, S. K. Kushwaha, T. Liang, et al., *Science* **350**, 413-416 (2015)

[46] Y. Ando, *J. Phys. Soc. Jpn.* **82**, 102001 (2013)

[47] Y. Zhang, Y.-W. Tan, H. L. Stormer, et al., *Nature* **438**, 201-204 (2005)

[48] K. S. Novoselov, A. K. Geim, S. V. Morozov, et al., *Nature* **438**, 197-200 (2005)

Figures

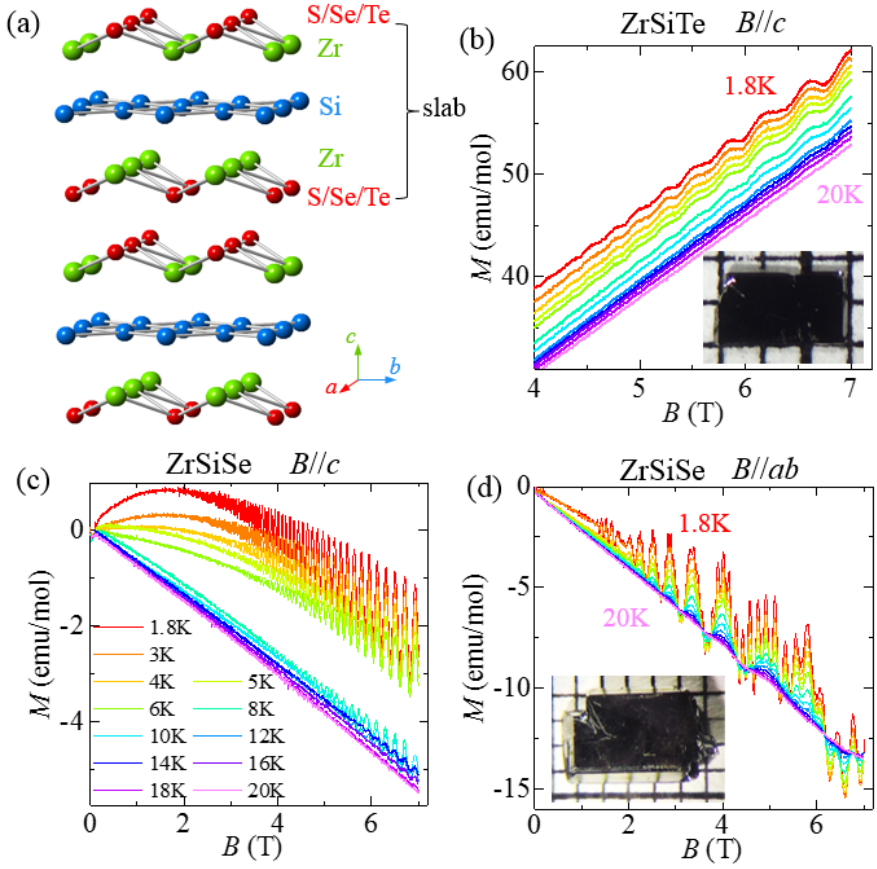

FIG. 1. (a) Crystal structure of ZrSiM (M=S/Se/Te). (b-d): Isothermal out-of-plane (*B*//*c*) magnetization for (b) ZrSiTe and (c) ZrSiSe, and in-plane (*B*//*ab*) magnetization for ZrSiSe (d) at various temperatures. The same temperature - color correspondence is used for these panels. Insets in (b) and (d), optical images of ZrSiTe and ZrSiSe single crystals.

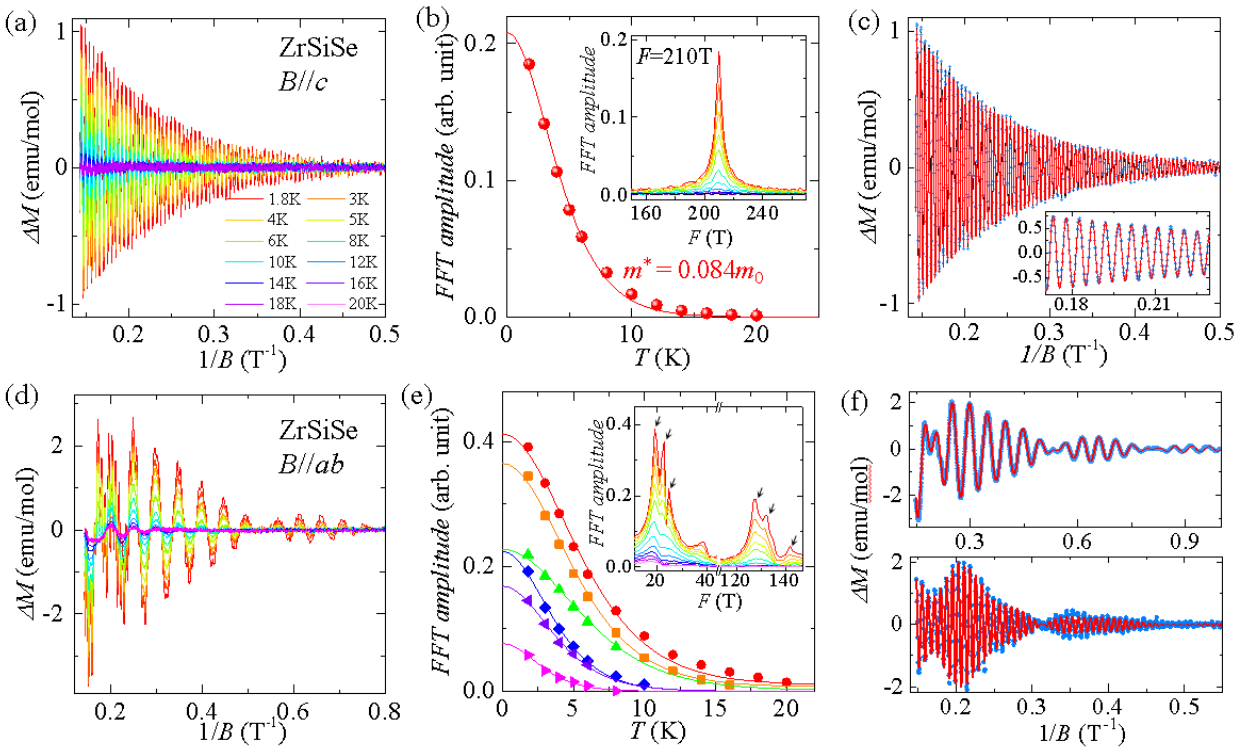

FIG. 2. (a) and (d): The oscillatory components of the (a) out-of-plane and (d) in-plane magnetization for ZrSiSe. (b) and (e): FFT amplitude vs. temperature; the solid lines represent the LK fits. Insets in (b) and (e), the FFT spectra of ΔM oscillations. The arrows in (e) indicate the FFT peaks. The peak near 40T is the harmonic peak. (c) The LK-fit (red line) of the out-of-plane oscillation pattern (blue points) at T=1.8K. Inset in (c), enlarged data and fitting. (f) The low- (upper panel) and high- (lower panel) frequency oscillatory components of the in-plane oscillations at 1.8K. The red solid lines represent the multiband LK-fits.

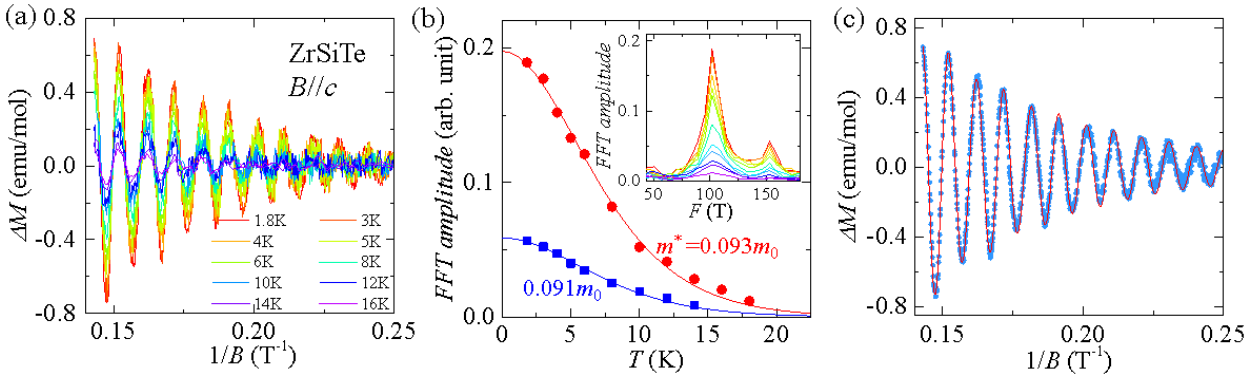

FIG. 3. (a) The oscillatory component of the out-of-plane magnetization for ZrSiTe. (b) FFT amplitude vs. temperature; the solid lines represent the LK fits. Inset, the FFT spectra of ΔM oscillations. (c) The fit (red line) of the oscillation pattern (blue points) at T=1.8K to the LK formula.

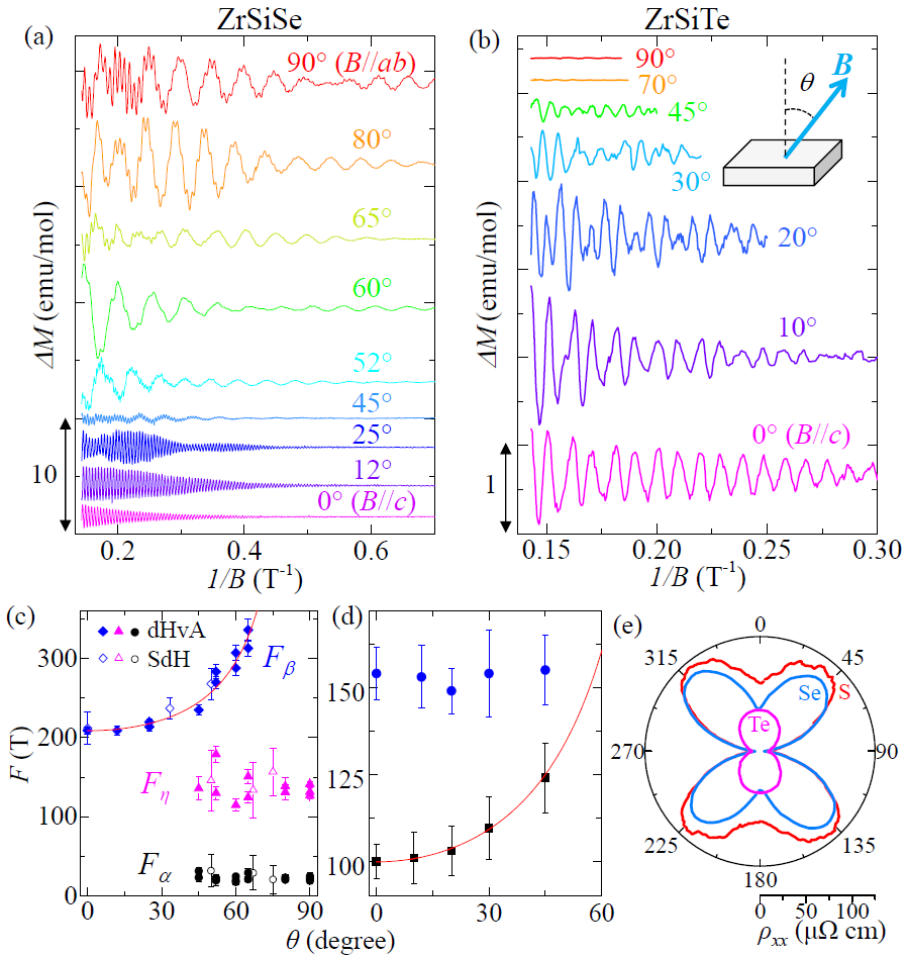

FIG. 4. (a-b): dHvA oscillations of (a) ZrSiSe and (b) ZrSiTe at T=1.8K under different magnetic field orientations. Inset in (b) shows the definition of field orientation angle θ. The data collected under at different θ have been shifted for clarity. (c-d): The angular dependences of the oscillation frequencies for (c) ZrSiSe and (d) ZrSiTe. Error bars are defined as the half-width at the half-height of FFT peaks. The red lines are fits to $F=F_{3D}+F_{2D}/\cos\theta$. (e) Polar plot of AMR at 9T for ZrSiS (red), ZrSiSe (blue) and ZrSiTe (magenta).

Table 1. Parameters derived from dHvA oscillations for ZrSiSe and ZrSiTe. F, oscillation frequency; T_D, Dingle temperature; m^*, effective mass; τ, quantum relaxation time; μ_q, quantum mobility; ϕ_B, Berry phase.

		F (T)	T_D (K)	m^*/m_0	τ (ps)	μ_q (cm^2/Vs)	ϕ_B		
							δ = -1/8	δ = 0	δ = 1/8
ZrSiSe	$B//c$	210	5.6	0.082	0.22	4605	0.31π		-0.19π
	$B//ab$	19.2	5.8	0.039	0.21	9461	1.17π	0.92π	0.67π
		22.8	8.2	0.042	0.15	6214	-0.31π	-0.56π	-0.81π
		24	11.1	0.037	0.11	5211	-0.35π	-0.6π	-0.85π
		126.9	10.8	0.059	0.11	3359	1.15π	0.9π	0.65π
		132.7	14.6	0.057	0.08	2572	-0.25π	-0.5π	-0.75π
		142	5	0.078	0.244	5488	-0.38π	-0.63π	-0.88π
ZrSiTe	$B//c$	102	14	0.093	0.086	1625	0.75π	0.5π	0.25π
		154	25	0.091	0.049	940	-0.15π	-0.7π	-0.95π